



ELSEVIER

Physica C 356 (2001) 239–253

PHYSICA C

www.elsevier.com/locate/physc

Microstructure and structural defects in MgB₂ superconductor

Y. Zhu^{a,*}, L. Wu^a, V. Volkov^a, Q. Li^a, G. Gu^b, A.R. Moodenbaugh^a,
M. Malac^a, M. Suenaga^a, J. Tranquada^b

^a Department of Applied Science, Materials Science Division, Brookhaven National Laboratory, Building 480, Upton, NY 11973, USA

^b Department of Physics, Brookhaven National Laboratory, Upton, NY 11973, USA

Received 16 May 2001; received in revised form 25 May 2001; accepted 25 May 2001

Abstract

We report a detailed study of the microstructure and defects in sintered polycrystalline magnesium diboride (MgB₂). Both transmission electron microscopy and X-ray data reveal that MgO is the major second-phase in our bulk samples. Although MgB₂ and MgO have different crystal symmetries, being P6/mmm and Fm-3m, respectively, their stacking sequence of Mg and B (or O) and lattice spacings in certain crystallographic orientations are very similar. The size of MgO varies from 10–500 nm, and its mismatch with the MgB₂ matrix can be a source for dislocations. Dislocations in MgB₂ often have a Burgers vector of $\langle 100 \rangle$, $1/3\langle 1-10 \rangle$ and $1/3\langle 210 \rangle$ partial dislocations and their associated stacking faults were also observed. Since both dislocations and stacking faults are located in the (001) basal plane, flux pinning anisotropy is expected. Diffuse scattering analysis suggests that the correlation length along the *c*-axis for defect-free basal planes is about 50 nm. (001) twist grain boundaries (GBs), formed by rotations along the *c*-axis, are major grain boundaries in MgB₂ as a result of the out-of-plane weak bonding between Mg and B atoms. An excess of Mg was observed in some grain boundaries. High-resolution nano-probe electron-energy loss spectroscopy reveals that there is a difference in near edge structure of the boron K-edge acquired from GBs and grain interiors. The change at the edge threshold may be suggestive of variation of the hole concentration that would significantly alter boundary superconductivity. © 2001 Elsevier Science B.V. All rights reserved.

Keywords: MgB₂; Microstructure; Defects; Crystal structure

1. Introduction

The recent discovery of the 39 K superconductivity in the binary intermetallic compound, magnesium diboride (MgB₂), by Akimitsu and co-workers [1] evoked a new enthusiasm for understanding the mechanism of superconductivity and

the structure–property behavior of this new class of materials. MgB₂ possesses the highest superconducting transition temperature *T_c* outside the cuprate- and C₆₀-related superconductors, and its superconductivity appears to follow the BCS theory, i.e., mediated via electron–phonon coupling. It was reported that the coherence length in MgB₂ is longer than that in the cuprates [2]. Also, unlike cuprates, grain boundaries (GBs) are strongly coupled and current density is determined by flux pinning [2,3]. Despite the phase inhomogeneity, porosity, untextured, nanoscale subdivisions of the

* Corresponding author. Tel.: +1-631-344-3057; fax: +1-631-344-4071.

E-mail address: zhu@bnl.gov (Y. Zhu).

not-yet-optimized MgB_2 ceramics, magnetization and transport measurements show that the polycrystalline samples can carry large current densities circulating over lengths of many grain sizes [3,4]. More recently, very high value of critical current densities as well as the critical fields were observed in thin films [5,6]. These properties hold tremendous promise for a wide range of large-scale and electronic applications, and suggest that the underlying microstructure can be intriguing. Immediately following the discovery, dozens of papers were published [1–13]; however, most of which dealing with synthesis, measurements of physical properties, and theory. There were few studies of microstructure and structural defects [11], which are extremely important for understanding the superconducting behavior. In this article, we report such an investigation using transmission electron microscopy (TEM) on sintered MgB_2 pellets. Structural defects, such as second-phase particles, dislocations, stacking faults, and grain boundaries were observed and analyzed using electron diffraction, electron-energy loss spectroscopy (EELS), high-resolution imaging, and structure modeling. Our analysis of the fundamental structural behavior in MgB_2 provides detailed insight on the microstructure and structure-properties relationship of the new superconductor not only for samples sintered under Mg vapor, but also for those fabricated via other synthesis procedures.

2. Sample preparation and magnetic properties

Bulk samples were prepared using commercial MgB_2 , which then was pressed into pellets 6 mm in diameter. The pellets were sealed into Al_2O_3 tubes with pure Mg and sintered under Mg vapor pressure of approximately 300 Torr at 1050°C for 24 h, followed by furnace cooling. The sintered pellets are gray and Mg-rich. Several center-cut and polished specimens were examined using an optical microscope, they appeared shiny and very dense (porosity is less than 5%) with average MgB_2 grain size of $\sim 10\ \mu\text{m}$. The superconducting properties were studied using a Quantum design MPMS SQUID magnetometer and standard four point

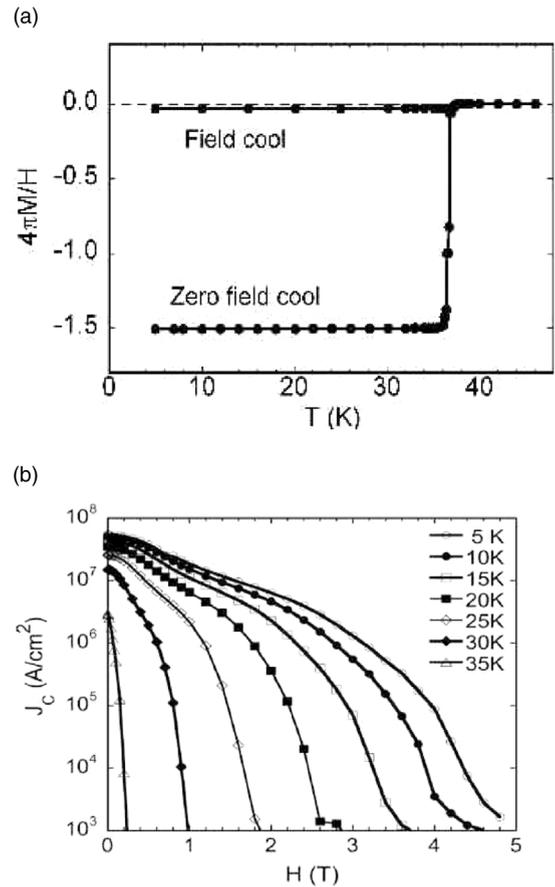


Fig. 1. (a) Magnetic shielding (zero field cool) and the Meissner effect (field cool) of the MgB_2 sample under external field of 2 Oe. (b) Magnetic field dependence of critical current density J_c of the MgB_2 sample at various temperatures.

transport measurements. Fig. 1(a) shows the shielding (zero field cool) and Meissner effect (field cool) of the MgB_2 specimen measured 2 Oe external field. The specimen has a sharp transition with mid-point $T_c = 37.2\ \text{K}$ and transition width of 0.7 K. A full bulk shielding ($\sim 100\%$) was observed after taking into account the demagnetization factor of the specimen.

Fig. 1(b) shows the magnetic field dependence of critical current density J_c of the specimen at various temperatures. This magnetically determined J_c was obtained by applying the standard Bean critical state model to the measured magnetic hysteresis of the specimen at applied external field up to 5 T, where the average grain size of $10\ \mu\text{m}$

was used. At 5 K and in self-field, the J_c for our specimen reaches as high as 5×10^7 A/cm². If the entire measured specimen dimension of ~ 2 mm is assumed, the value of J_c is scaled down by a factor of approximately 200. Then, the corresponding value of J_c at 5 K and self-field would be 2.5×10^5 A/cm², which is comparable to that reported by other groups in the literature [2,3,8].

A standard θ – 2θ X-ray powder diffraction technique was used to identify the bulk phase, composition and lattice parameter. X-ray diffraction patterns were collected with Cu K α radiation ($\lambda = 0.154178$ nm) over a 2θ range from 10° to 100° at a step width of 0.02° , after a diffracted beam monochromator. Detailed microstructure and structural defects were characterized using a JEOL3000F electron microscope with a field-emission source operated at 300 kV. After mechanical polishing down to a thickness of 15 μ m, TEM samples were prepared via a standard ion-milling procedure at 3.5 kV and 10° glancing angle at liquid N₂ temperature. The microscope has an image resolution of 0.165 nm and energy resolution of 0.7 eV. The data acquisition system is equipped with a TV-rate camera, a slow scan CCD and Fuji Imaging Plates. The CCD camera is integral to the Gatan energy filter and energy-loss spectrometer. For chemical analysis, we used both energy-dispersive X-ray (EDX) spectroscopy and

EELS. Since both boron and magnesium ($Z = 5$ and 12, respectively) are light elements, EELS has much higher sensitivity to probe them than EDX does. Furthermore, the absorption of electron-induced soft X-rays from light elements poses a significant limitation on quantitative EDX analysis. Thus, we relied heavily on EELS for our chemical analyses. Steps were taken to minimize contamination which might affect nanoprobe characterization. The samples were examined either at liquid N₂ temperature or, if at room temperature, underwent a plasma cleaning process for 20–30 min using argon and oxygen gases which significantly reduced carbon contamination.

3. Microstructure and structural defects

3.1. Microstructure

Fig. 2 shows the X-ray diffraction spectrum of the powder sample ground from a sintered pellet. All the reflections can be unambiguously indexed to three phases, with roughly 70% of MgB₂ and 30% of periclase (MgO) and metal magnesium. No other phases, such as MgB₄ and MgB₇, were detected. The lattice parameters for MgB₂ were determined to be $a = 0.3086(5)$ nm and $c = 0.3518(5)$ nm, consistent with Ref. [1]. Metal–magnesium–metal was not observed in the TEM samples; it

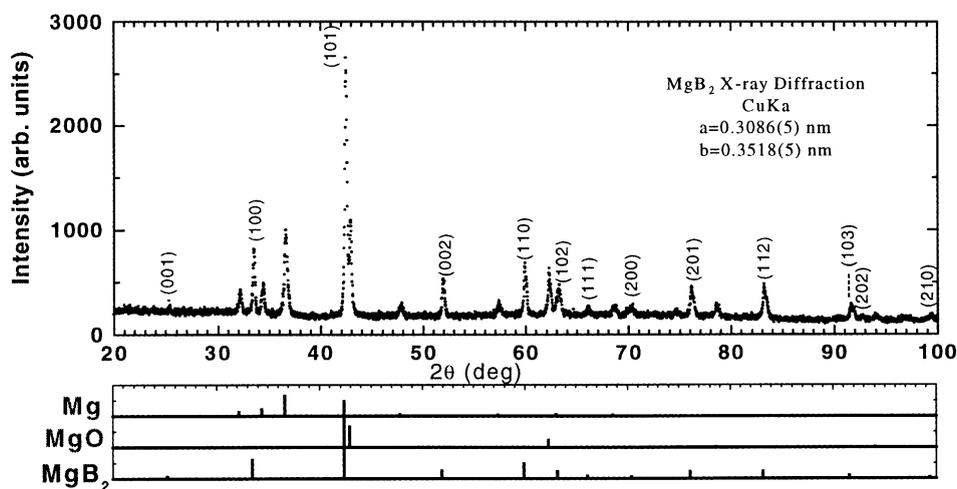


Fig. 2. X-ray diffraction measurements showing a mixture of MgB₂, MgO, and Mg in the sample. The diffraction peaks are indexed to MgB₂, and the peak positions of all three phases are marked below.

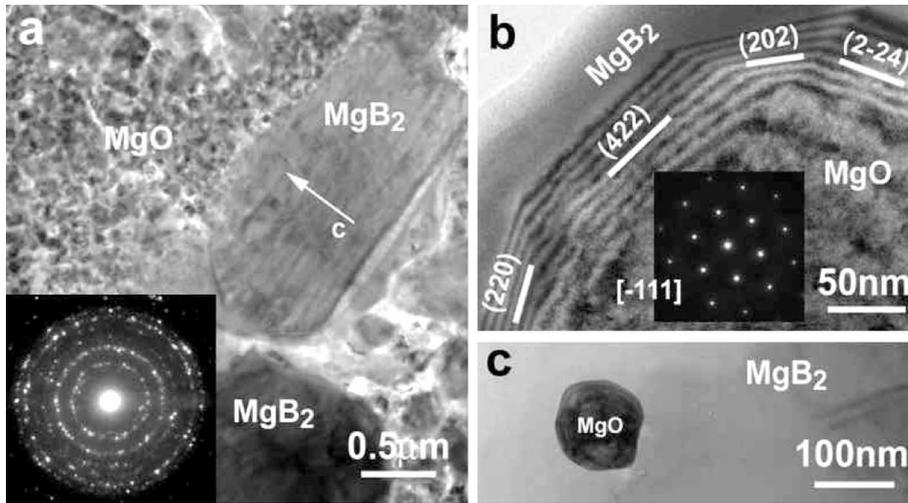


Fig. 3. MgO second-phase particles in MgB₂. (a) Small aggregated MgO particles solidified from MgO vapor and their corresponding diffraction ring-pattern; the nearby MgB₂ platelet exhibits faceting along the basal plane. (b) A large MgO particle viewed along the $[-111]$ threefold axis showing faceting parallel to the 220 and 422 lattice planes. (c) An isolated small MgO particle embedded in MgB₂ showing little strain contrast at the interphase interface.

was probably oxidized during the ion-milling and plasma-cleaning processes. TEM reveals that MgB₂ has space group P6/mmm, possessing a simple hexagonal structure common among the borides [14], being consistent with our X-ray diffraction observations. This crystal structure consists of honeycomb-net planes of boron, separated by triangular planes of Mg, with the center of a boron honeycomb lying both directly above and below each Mg atom. In Fig. 2 and in the following analysis, the three-index notation, hkl , is used to index the MgB₂ crystal. Although the four-index notation, $hkil$, brings in the sixfold crystal symmetry, it does not directly represent the reciprocal relation between diffraction and image which is particularly important for TEM. In the three-index system, a reciprocal vector is always perpendicular to its corresponding lattice plane, but not necessary parallel to the direction vector of the same index in real space.

Generally, the individual MgB₂ crystals (or grains) of our samples seemed rather clean and dense, as suggested by their sharp Kikuchi lines shown in convergent beam diffraction. However, because of the existence of the aggregates of solidified MgO and many poorly sintered, and poorly connected MgB₂ grains (Fig. 3a), overall the

samples were mechanically weak. Some parts appeared porous and crumbly, similar to the sintered, oxygen-deficient, bulk samples of YBa₂-Cu₃O_{7- δ} ($\delta > 0.5$) as assessed by mechanical polishing and optical microscopy. We take advantage of the small probe of TEM and focus on stoichiometric MgB₂ grains that act like single crystals under our microscope. The majority of the MgB₂ grains we observed are faceted along the basal plane, and many of them are shaped like platelets with an aspect ratio of about 1:3 (Fig. 3a), suggesting a two-dimensional character consistent with the layered nature of the structure. The long axis of the platelets is about 2 μ m on average. For grains without such a shape, the averaged size is about 1.5 μ m. Few crystal grains are free of defects. The major defects in MgB₂ crystals are second-phase particles, dislocations, including stacking faults associated with partial dislocations, and GBs. We discuss the observations and analysis of these defects below.

3.2. Second-phase particles

The major second phase in our samples is MgO, although particles containing other elements, such

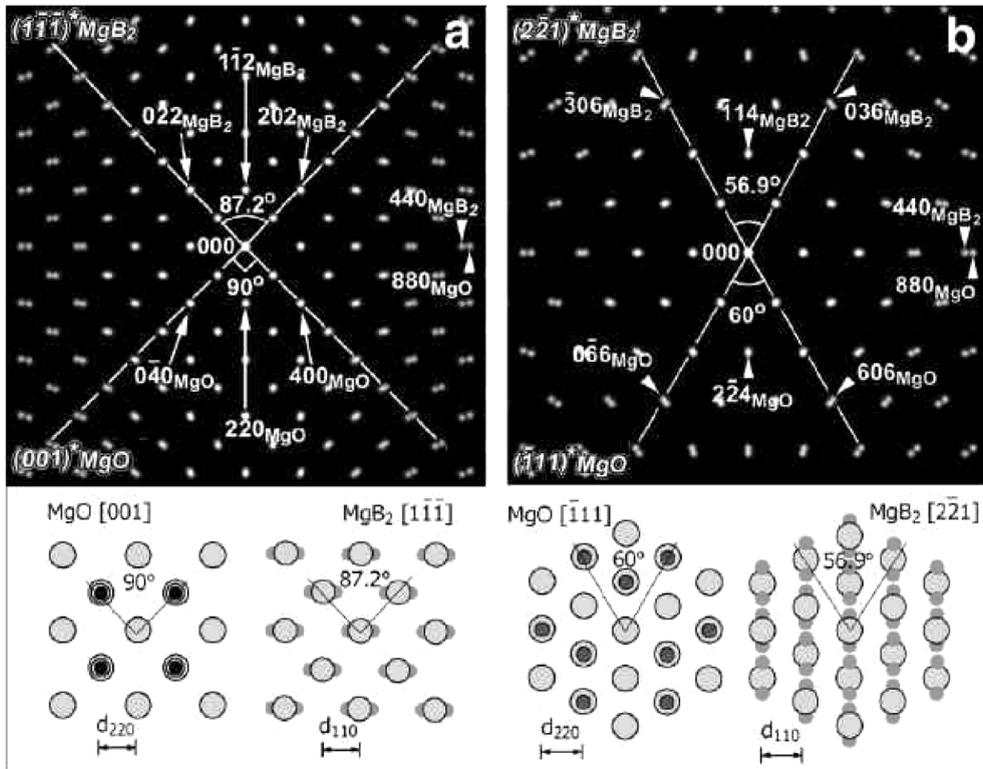


Fig. 4. Structural similarity of MgB_2 and MgO in two crystallographic orientations. (a) Superimposed diffraction patterns of $(001)_{\text{MgO}}^*$ and $(1-1-1)_{\text{MgB}_2}^*$; configurations of Mg and B layers projected along the $[001]_{\text{MgO}}$ and $[1-1-1]_{\text{MgB}_2}$ directions are shown below. Lattice spacing: $d_{2-20(\text{MgO})} = 0.1489$ nm, $d_{1-12(\text{MgB}_2)} = 0.1470$ nm, $d_{220(\text{MgO})} = 0.1489$ nm, and $d_{110(\text{MgB}_2)} = 0.1543$ nm. (b) Superimposed diffraction patterns of $(-111)_{\text{MgO}}^*$ and $(2-21)_{\text{MgB}_2}^*$, with configuration of the Mg and B layers projected along the $[-111]_{\text{MgO}}$ and $[2-21]_{\text{MgB}_2}$ directions. Lattice spacing: $d_{2-24(\text{MgO})} = 0.0860$ nm, $d_{-114(\text{MgB}_2)} = 0.0836$ nm, $d_{220(\text{MgO})} = 0.1489$ nm, and $d_{110(\text{MgB}_2)} = 0.1543$ nm.

as Fe, were also observed. The impurity atoms likely come from the original commercial powder. The size of the MgO particles had a wide distribution, ranging from 10 to 500 nm (Fig. 3a–c). The large ones often assemble the MgB_2 grain, although MgO grains can be faceted along the 220 and 422 planes (Fig. 3b). Both X-ray and TEM diffraction show that MgO has fcc structure belonging to space group of Fm-3m. Despite the different crystal symmetries of MgO and MgB_2 , cubic and hexagonal, respectively, their diffraction patterns in some orientations look identical (Fig. 4a and b), so that the same crystal must be tilted to different zone axes and its symmetry then examined to unambiguously distinguish between MgO and MgB_2 . For example, even with the presence of the unique dumbbell configuration for MgB_2 in the

hexagonal structure, the lattice symmetry and in-plane spacings projected along the $[1-1-1]$ and $[2-21]$ directions are very similar to those of MgO projected along the $[001]$ and $[-111]$ directions, respectively (Fig. 4). Fig. 4a shows a calculated diffraction pattern superimposing $\text{MgB}_2 (1-1-1)^*$ on $\text{MgO } (001)^*$. We see that all of the low-order reflections are coincident. The notable difference is the intercept angle of the ‘square’ lattices (as marked in Fig. 4a and b). The angle for MgO projected along the $[001]$ is 90° , while for MgB_2 along the $[1-1-1]$ direction is $90^\circ \pm \alpha$, where $\alpha = 2.8^\circ$. A similar situation exists for the projected lattice plane for $[-111]_{\text{MgO}}$ and $[2-21]_{\text{MgB}_2}$. The former has a true threefold symmetry, while the latter has an intercept angle $60^\circ \pm \beta$ with $\beta = 3.1^\circ$. In both cases, the difference in their

corresponding lattice spacings is negligibly small. For example, $d_{220(\text{MgO})} = 0.1489$ nm, $d_{1-12(\text{MgB}_2)} = 0.1470$ nm; $d_{224(\text{MgO})} = 0.0860$ nm and $d_{-114(\text{MgB}_2)} = 0.0836$ nm. Such orientation relationships may imply the possible low-energy epitaxial growth of the two phases and the existence of good lattice-match at the MgO and MgB₂ interfaces, as seen in Fig. 3c where the interfacial misfit dislocations and the associated strain are not visible. Care has to be taken to identify them. For small particles where systematic tilt is not feasible, EDX and EELS can be used to distinguish MgO from MgB₂. As seen in Fig. 5, besides the pronounced K-edge of boron at 188 eV and of oxygen at 532 eV for MgB₂ and MgO, respectively, the Mg core-loss fine structure is also different for the two, suggesting the difference in bonding characteristics of magnesium with boron and oxygen. The insets of Fig. 5 show the Mg K-edges after background subtraction. For clarity, the core-loss intensity of the Mg edge in Fig. 5b was amplified by a factor of 8.5.

3.3. Dislocations and stacking faults

Dislocations are the predominant defects in MgB₂. Most of them are perfect dislocations with

mixed edge and screw components lying in the a - b basal planes normal to the c -axis. They sometimes interact with second phase particles. Fig. 6(a–d) shows diffraction contrast of the same area containing straight dislocations, dislocation loops and MgO particles. The images were recorded from the same area near the $[10-1]$ direction, i.e., 41° off the $[001]$ direction, with different operating reflections. Characterization using the $\mathbf{g} \cdot \mathbf{b}$ extinction rule suggests that most are screw dislocations with a Burgers vector of $[100]$, and as evident when $\mathbf{g} = 010$ was used, they are out-of-contrast (Fig. 6d). The particles marked by black arrows in Fig. 6a are MgO. Thickness fringes observed within the particles suggest they are spherical in shape. Dislocation loops and partial dislocations, both bonding stacking fault and lying in the basal plane, are also present, as marked by small arrows in Fig. 6b. The displacement vector of the stacking fault associated with the dislocation loops apparently differs from the Burgers vector of the dislocations that bond them, based on the diffraction contrast under different imaging conditions. Fig. 7 are basal-plane dark-field (DF) images (viewed along the c -axis), showing the interaction of dislocations and two small MgO particles, each about

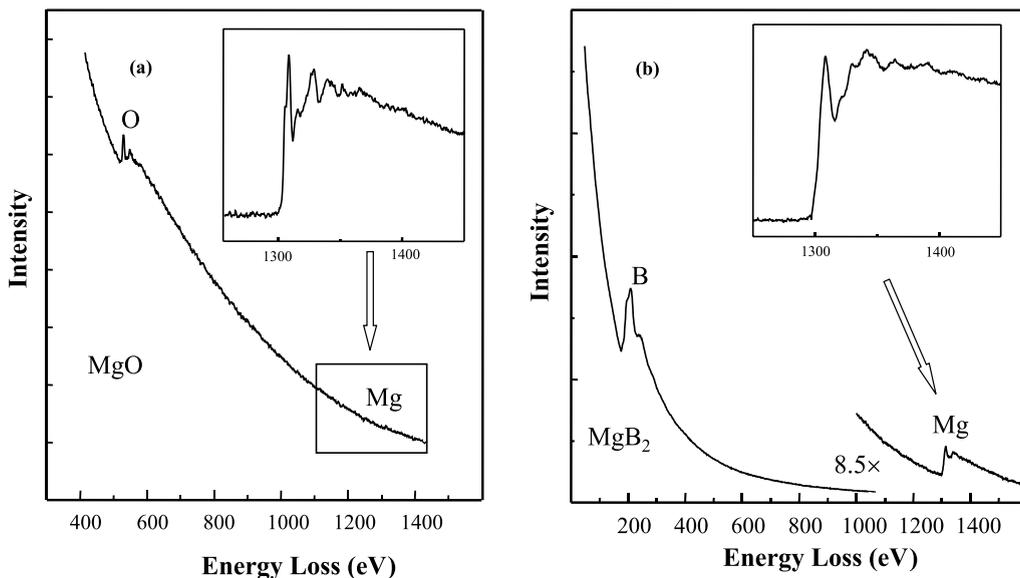


Fig. 5. EELS spectra from (a) MgO, and (b) MgB₂ with the Mg intensity magnified by a factor of 8.5. The insets show the enlarged Mg K-edge after background subtraction.

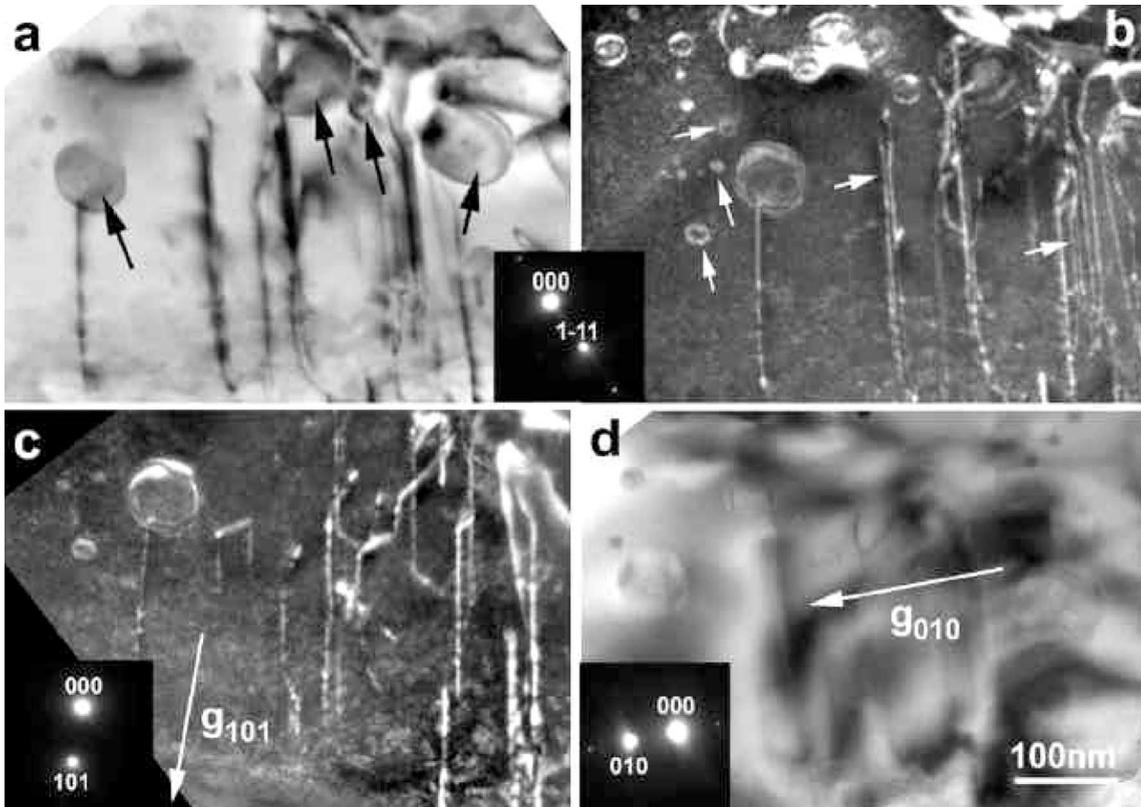


Fig. 6. Structural defects in MgB_2 . Images from the same area using different operating reflections. (a) Bright-field image with $g = 1-11$ reflection, (b–d) dark-field image using $g = 1-11$ reflection (b), $g = 101$ reflection (c) and $g = 010$ reflection (d). Note, most of the defects are out of contrast in (d). Large arrows indicate MgO particles and small arrows indicate dislocation loops. Partial dislocations are also visible.

24 nm in diameter. The inset of Fig. 7(a) is the DF image of one of the particles recorded using the MgO 400 reflection. Tilting experiments reveal that these are perfect dislocations gliding in the basal plane. When the 030 reflection was used, the dislocations are out-of-contrast, suggesting a $[100]$ Burgers vector. Diffraction analysis reveals an orientation relationship between the two phases with $(111)_{\text{MgO}} \parallel (101)_{\text{MgB}_2}$, resulting an in-plane lattice mismatch of $\delta = 14\%$. The origin of the dislocation nucleation and propagation associated with the imbedded MgO particles can be attributed to the interfacial strain cause by different thermal contraction rates of MgO and MgB_2 and the stiffness of the a – b lattice in MgB_2 . This is consistent with Jorgensen et al.'s observations that MgB_2 has unusually large anisotropies with larger

thermal expansion and compressibility along the c -axis, but not in the basal plane [9].

Fig. 8 shows dislocation images viewed along a direction orthogonal from those shown in Fig. 7. Here the a – b planes are viewed nearly edge-on. The line contrasts in Fig. 8 are attributed to dislocations lying in the a – b plane. When $g = 002$ was used, the line contrast disappeared, suggestive of an in-plane Burgers vector. However, a detailed analysis shows that these are not screw dislocations, but are general dislocations in the a – b plane, running from the top to the bottom surfaces of the sample, as evident by the intensity oscillation that is associated with the thickness extinction along the dislocations. In the $[010]$ zone axis (Fig. 8a), the line contrast represents the projected dislocation contrast in the basal plane. In the area of

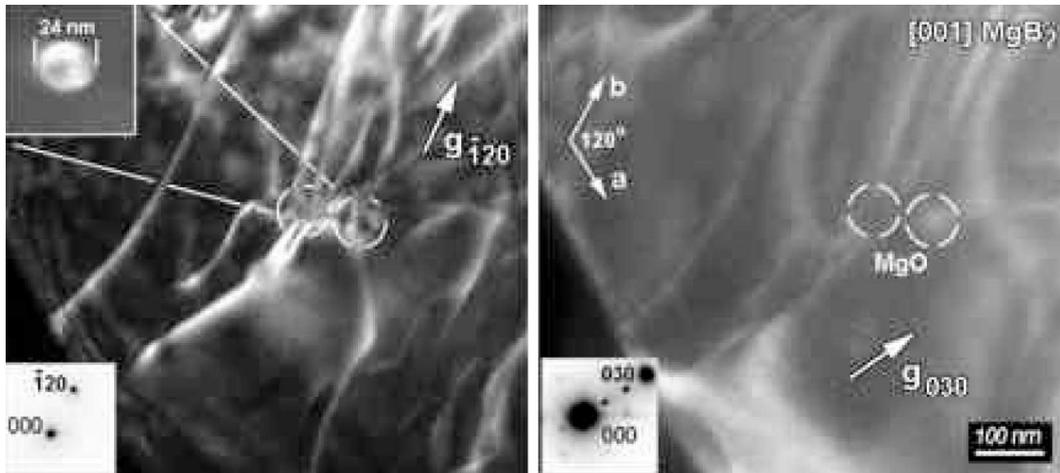


Fig. 7. Dark-field images, viewed near along the c -axis of MgB_2 crystal with MgO particles as a nucleation center for dislocations. (a) With $\mathbf{g} = -120_{\text{MgB}_2}$ reflection: there are two adjacent particles in the area, one imaged using the $\mathbf{g} = 400_{\text{MgO}}$ reflection is shown in inset. (b) With $\mathbf{g} = 030_{\text{MgB}_2}$ reflection: dislocations are out of contrast, while the particles are still visible.

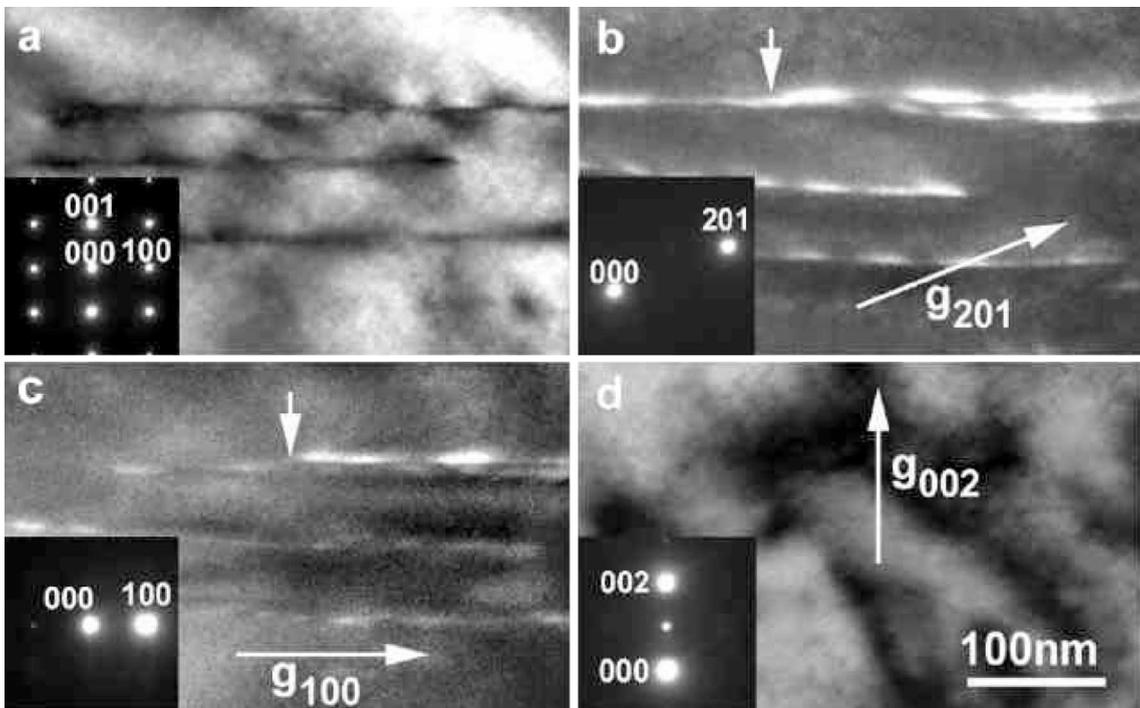


Fig. 8. A partial dislocation associated with a stacking fault (marked by an arrow) viewed with the basal plane near edge-on. All the corresponding diffraction patterns are shown in insets. (a) The basal planes are viewed exactly edge-on. (b–d) the basal plane was tilt away $\sim 10^\circ$ from the zone axis. The dissociation of a perfect dislocation into two partials is clearly visible with the 201 reflection (b) and the 100 reflection (c), but invisible with the 002 reflection (d).

Fig. 8b, marked by an arrow, we see the dissociation of a perfect dislocation into two partials. We note that the double line-contrast cannot be attributed to dynamic diffraction because the split is visible (Fig. 8c) even when the imaging conditions $\mathbf{g} \cdot \mathbf{b} < 2$ were used [15]. Apparently the dissociation is due to the lattice shift in the basal plane.

In Fig. 9, we propose structural models for perfect dislocations and partial dislocations involving both Mg and B sublattices in the system. Fig. 9a represents a model for an edge dislocation with a Burgers vector of [100] lying in the basal plane as observed in the experiments. In this case, the lattice shift induced by a dislocation is over two sublattices spacings, i.e., either Mg \rightarrow Mg, or B \rightarrow B. For clarity, Fig. 9a shows the projected a - c plane and a - b plane of the MgB_2 , where the small dots represent B atoms, while the big gray and black dots represent Mg atoms at different depth in the crystal. Based on this model, the presence of the edge dislocation can be imagined as the insertion of two Mg–B half-planes with a total spacing of $a = 0.308$ nm numerically equal to the modulus of Burgers vector of $\mathbf{b} = [100]$. Fig. 9b illustrates the dissociation of a perfect $\mathbf{b} = [100]$ edge dislocation into two Shockley partial dislocations with Burger vectors $\mathbf{b}_1 = 1/3[1 - 10]$ and $\mathbf{b}_2 = 1/3[210]$, bounding a stacking fault in between. Here, we assign A, B, C as magnesium sites and α, β, γ as boron sites, as depicted in Fig. 9c. The diagrams (Fig. 9c–e) explain how the partials with Burgers vector $\mathbf{b}_1, \mathbf{b}_2$, or \mathbf{b}_3 change the stacking sequence along the c -axis in a hexagonal crystal. Using this notation the formation of planar fault caused by the dislocation reaction $\mathbf{b} = [100] = \mathbf{b}_1 + \mathbf{b}_2 = 1/3[1 - 10] + 1/3[210]$ can be expressed as:

$$\begin{aligned} & \dots A(\beta\gamma)A(\beta\gamma)A(\beta\gamma)|A(\beta\gamma)A(\beta\gamma)A(\beta\gamma) \dots \\ \mathbf{b}_1 : & |B(\gamma\alpha)B(\gamma\alpha)B(\gamma\alpha)B(\gamma\alpha) \dots \\ \mathbf{b}_2 : & |A(\beta\gamma)A(\beta\gamma)A(\beta\gamma) \dots \end{aligned}$$

That is, after the dissociation, the stacking sequence shifts back to its original. This is similar to Shockley partials in simple fcc structures. The energy associated with the dissociation can be expressed as $E_{\mathbf{b}} = E_{\mathbf{b}_1} + E_{\mathbf{b}_2} + E_{\text{SF}}$. Since $E_{[100]} > E_{1/3[1-10]} + E_{1/3[210]}$, it implies that the reaction is

energetically favorable, and the energy difference is balanced by the energy of the stacking fault E_{SF} ($E_{\text{SF}} = we_{\text{SF}}$, where w and e_{SF} are the width and energy per unit length, respectively, of the stacking fault). Since experimentally, only narrowly spaced partial pairs (Figs. 6b, 8b and c) were observed, a large value of e_{SF} is suggested. The possible dissociation for other equivalent perfect dislocations can be derived using a general diagram shown in Fig. 9e.

The motion of the partial dislocations and the associated stacking fault we described above is conservative. However, a non-conservative fault can also be formed if there is a missing a - b plane of boron or an intercalation of an a - b plane of magnesium at the fault. The situation for the lattice shift is the same for the stacking fault described in Fig. 9, except it forms a local magnesium structure. Magnesium is a hcp crystal with the lattice parameter $a = 0.32$ nm, very similar to the lattice parameter $a = 0.31$ nm for MgB_2 . The stacking fault associated with the dislocation loop we observed (Fig. 6) belongs to this type. The formation of such loops (Frank dislocation loops) can be attributed to the excess Mg in our samples.

The distribution of the faulted basal planes due to the dislocations and stacking faults is best seen when the a - b planes are viewed edge-on, the grains B and C in Fig. 10 serving as examples. Electron diffraction, using parallel illumination of a large area similar to grain B, recorded on an image plate, revealed a broadening of the Bragg spots along a direction perpendicular to the basal plane (Fig. 10d). A line scan of the intensity of 300 reflection is shown Fig. 10e. The reflection intensity can be fitted into two profiles; one is a mixture of Gaussian and Lorentzian distribution attributed to the Bragg peak, the other is a Gaussian distribution associated with diffuse scattering. The width of the diffuse scattering peak gives an average of 50 nm correlated length, i.e., the averaged distance from one non-faulted basal plane to the next.

3.4. Grain boundaries

There are two types of GBs in our samples. One represents poorly coupled grains with amorphous

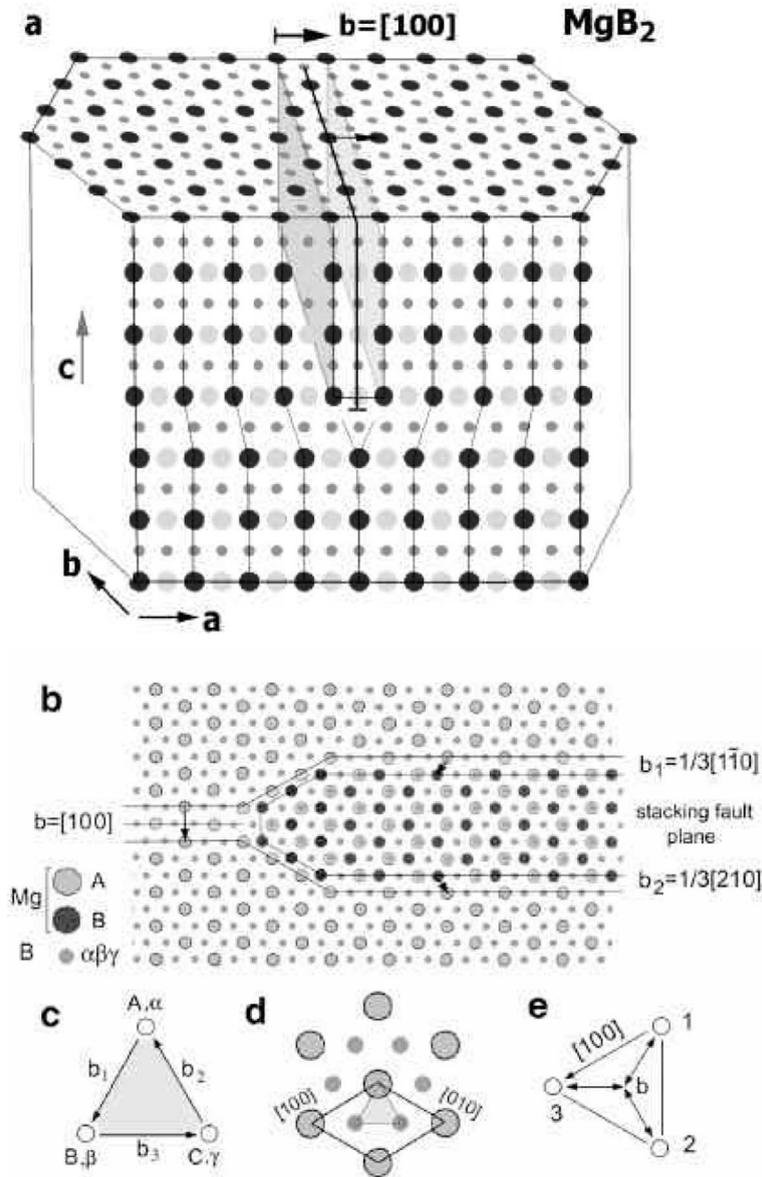


Fig. 9. (a) Structural model for a perfect edge dislocation with a Burgers vector $\mathbf{b} = [100]$. The small and big dots represent B and Mg atoms, while the dark and gray color of the big dots represent the Mg at different depths. (b) Structural model for the dissociation of a perfect dislocation into two partials: $\mathbf{b} = [100] = \mathbf{b}_1 + \mathbf{b}_2 = \frac{1}{3}[1\bar{1}0] + \frac{1}{3}[210]$. The stacking sequence across the fault is: $\dots A(\beta\gamma)A(\beta\gamma)A(\beta\gamma)|B(\gamma\alpha)B(\gamma\alpha)|A(\beta\gamma)A(\beta\gamma)A(\beta\gamma) \dots$ where A and B denote the magnesium sublattice and $\alpha\beta\gamma$ the boron sublattice, as depicted in (c–e). For details, see text.

material at the boundaries, while the other type involves well-coupled grains with structurally intact boundaries, marked as 1 and 2 in Fig. 10a, respectively. The amorphous boundary in Fig. 10a

is a tilt boundary with the basal plane of one of the constituent grains as its boundary plane. The two grains across the boundary are rotated 45° about the $[010]$ axis, as is evident from the line contrast

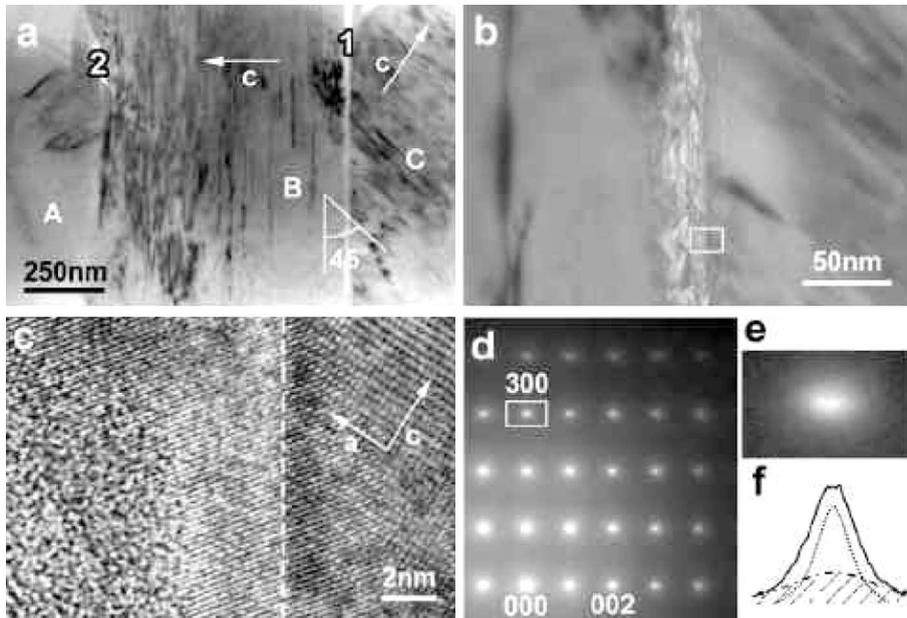


Fig. 10. (a) Three grains with two typical GBs in MgB_2 . 1: amorphous boundary, and 2: structurally intact boundary. The dense parallel line contrast across the amorphous boundary corresponds to the projected basal planes. (b) Enlargement of the amorphous boundary. (c) HRTEM of enlarged box area in (b) showing local crystalline region in the amorphous layer. (d) Diffraction pattern covering an area similar to the grain B in (a) showing a broadening of the Bragg reflections in the direction perpendicular to the basal planes. (e) Enlargement of reflection of 300 and (f) its intensity profile fitted with the Bragg intensity and diffuse scattering (shaded area).

due to the faulted a - b planes (Fig. 10a and b). Although the boundary is amorphous overall, local crystalline areas are also visible, often having an epitaxial relationship with the crystal grain, as shown in Fig. 10c (the dashed vertical line indicates the interface between left grain and the thick amorphous boundary). As discussed later, these crystalline areas are likely to be MgO. The thickness of the amorphous layer at such boundaries ranges from 10–50 nm.

For structurally intact GBs, we observed many (001) twist boundaries, both large-angles and small-angles, with an in-plane rotation about the c -axis across the interface, similar to the GBs in the $\text{Bi}_2\text{Sr}_2\text{CaCu}_2\text{O}_8$ superconductor. This can be attributed to the layered nature of the MgB_2 structure, with graphite-like boron layers which are separated by hexagonal close-packed layers of Mg. It is consistent with the prediction that the B–B bonds in the basal plane are much stronger than the Mg–B bonds that connect layers of Mg

and B atoms [9]. The lattice distortion associated with such boundaries often extends only a few atomic layers and their interfacial structure can be retrieved at different length scales using diffraction contrast, as well as by high-resolution imaging. An example of a 4.1° small-angle (001) GB is shown in Fig. 11. Fig. 11a displays a two-beam image of the boundary showing the diffraction contrast of the quasi-periodic dislocation array at the interface. Fig. 11b is a high-resolution (002) lattice image showing alternating Mg–B layers running across the boundary. As characterized by Kikuchi patterns, the major components of the boundaries are the 3.7° twist component about the [001] axis and a small tilt component 0.8° about the [120] axis. A careful examination of the Kikuchi pattern reveals another tilt component of 1° about the [100] axis which is accommodated by inserting extra a - b planes (marked as an edge dislocation in Fig. 11c) at the boundary. Based on the Frank formula, $d = \sin \theta / b$, where b is the amplitude of

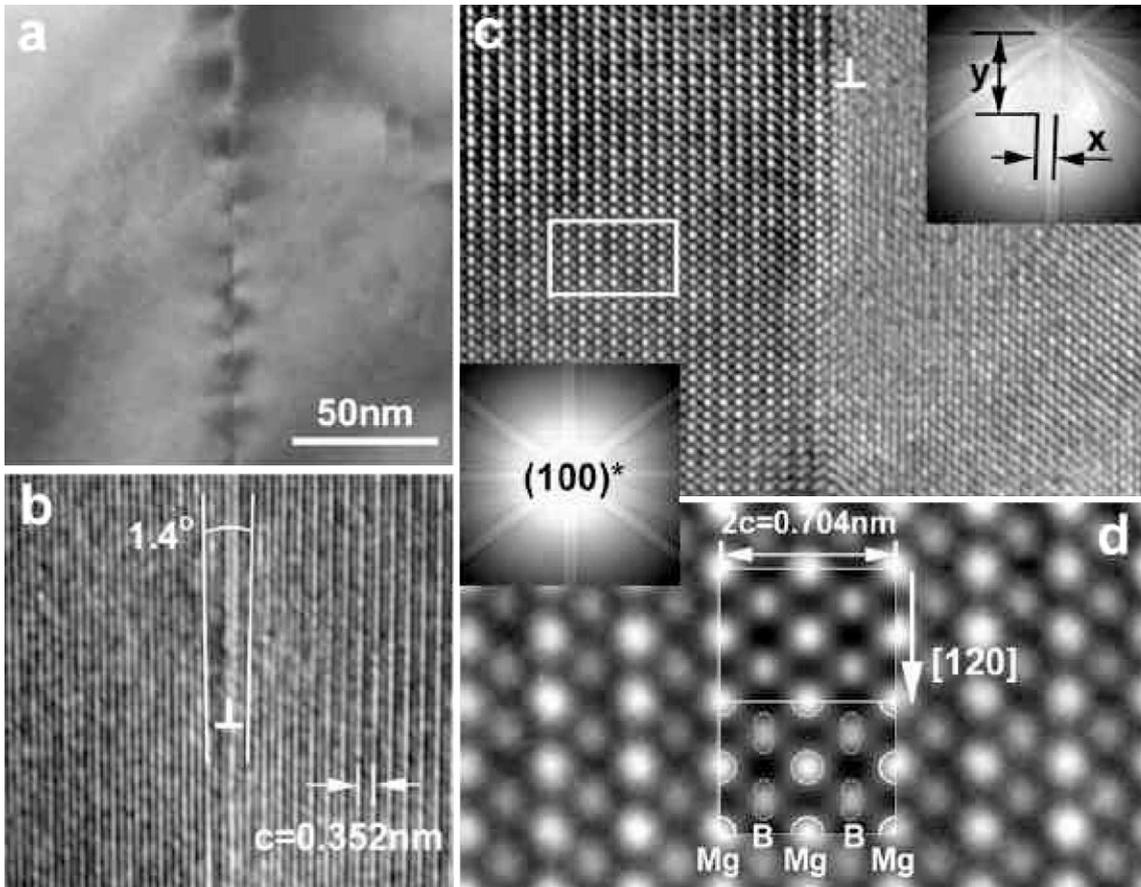


Fig. 11. A 4.1° small-angle (001) GB in MgB_2 . (a) Diffraction contrast associated with interfacial dislocations. (b) Both crystals were tilted away from any zone axes, showing clearly the alternating Mg–B layers (the (002) lattice fringes) and the 1.4° tilt component. (c) The left crystal was tilted to the [100] direction, so both Mg and B atoms are clearly visible. The Kikuchi patterns acquired from both crystals are also included to show the exact misorientation of the GB ($x = 0.8^\circ$, $y = 3.7^\circ$). (d) Enlarged box area of (c) showing the arrangement of B and Mg atoms. The embedded image is the calculated one for defocus value $\Delta f = -60$ nm and thickness $t = 3$ nm, where the Mg atoms are seen as bright dots, while the B atoms are weak white dots.

Burgers vector of the edge dislocations, θ the tilt angle, and d the dislocation spacing, the calculated dislocation spacing (14 nm) and Burgers vector [001] are consistent with our experimental observations. The other components of the boundary may be accommodated by two sets of interfacial screw dislocations, which are not visible in the images (Fig. 11a–c) when they are not viewed edge-on. In Fig. 11c, the [100] direction of the left crystal was tilted parallel to the incident beam, while the right crystal was off the [100] axis. A high-resolution image of the boxed area in Fig. 11c is shown in Fig. 11d, where the Mg atoms are

viewed as bright dots and B atoms weak white dots. The embedded image is a simulated one with four unit-cells in the projection, showing good agreement with the experiment. The projected boron dumbbell with a spacing of 0.089 nm is not resolved in the image.

Quantitative nano-probe EELS was carried out on several GBs and compared with the results from grain interiors (GIs). To achieve a small probe with sufficient beam current and energy resolution, the microscope was set in the nano-beam-diffraction (NBD) mode with a nominal probe size of 0.6 nm (the actual FWHM of the

probe is about 1 nm), and a collection angle of 10 mrad. To improve the signal/noise ratio, the spectra were acquired in diffraction mode using an accumulative acquisition method with the maximum intensity in each acquisition being just slightly below the saturation of the CCD camera.

Initial elemental quantification was done by standard power-law background subtraction at the elemental edges, followed by integration of the core-loss intensity to obtain the intensity ratio, such as I_K^{Mg}/I_K^B . The formula $N^{Mg}/N^B = (I_K^{Mg}/I_K^B)(\sigma_K^B/\sigma_K^{Mg})$ was used to obtain the areal concentration ratio, N^{Mg}/N^B . The K-ionization cross-sections were calculated using the hydrogenic approximation for generalized oscillator strength [16]. For $E_0 = 300$ keV and $\beta = 10$ mrad, we obtain $\sigma_K^B/\sigma_K^{Mg} = 86.64$ for an energy window $\Delta = 50$ eV, and $\sigma_K^B/\sigma_K^{Mg} = 97.98$ for $\Delta = 30$ eV. Although a larger window is more susceptible to the errors due to the background subtraction, it is less sensitive to the near-edge fine structure. The averaged integrated intensities using both windows were used. Tables 1 and 2 list the variation of concentration ratios for the structurally intact boundaries and amorphous boundaries, respectively.

Most of the quantitative measurements were obtained from thin regions with a thickness about $0.5\lambda_m - \lambda_m$ (where λ_m is the inelastic mean-free-path). Table 1 gives the concentration ratio of N^{Mg} to N^B for three structurally intact boundaries of MgB_2 using 1 nm-probe EELS, where GB denotes the grain boundary and GI denotes the grain interior about 100 nm away from the boundary. Each measurement represents an average of five data points. For GB I and GB II, we observe a $\sim 50\%$ increase in Mg/B ratio at the boundaries, while in GB III we saw no significant change. Evidently, Mg segregation at the boundaries is sensitive to local structure. The relation to the boundary geometry including misorientation angle and core-structure of interfacial dislocations will be the subject of a further study. However, it is important to note that these non-stoichiometric GBs are similar to those found in Nb_3Sn [17,18] and can be the site of strong flux pinning when the grain sizes are significantly reduced [5].

At amorphous boundaries (Table 2), besides seeing variation of Mg, we observed a significant

Table 1
EELS measurements of boron and magnesium concentration ratio at structurally intact GBs and GIs^a

	I^{Mg}/I^B ($\times 10^{-2}$)	N^{Mg}/N^B	$(N^{Mg}/N^B)^{GB}/(N^{Mg}/N^B)^{GI}$
GB I	3.7	3.24	1.64
GI I	2.3	1.98	
GB II	3.5	3.00	1.44
GI II	2.4	2.09	
GB III	2.5	2.15	1.06
GI III	2.3	2.03	

^a The core-loss cross-section ratios $(\sigma_K^B/\sigma_K^{Mg})_{\Delta=30 \text{ eV}} = 0.98 \times 10^2$ and $(\sigma_K^B/\sigma_K^{Mg})_{\Delta=50 \text{ eV}} = 0.87 \times 10^2$ were calculated for 300 keV electrons at an collection of 10 mrad.

Table 2
EELS measurements of boron and oxygen concentration ratio at amorphous GBs and GIs^a

	I^O/I^B	N^O/N^B
GB I	6.7×10^{-2}	0.702
GB II	4.3×10^{-2}	0.451
GI	3.7×10^{-3}	0.038

^a The core-loss cross-section ratios $(\sigma_K^B/\sigma_K^O)_{\Delta=30 \text{ eV}} = 9.98$ and $(\sigma_K^B/\sigma_K^O)_{\Delta=50 \text{ eV}} = 9.16$ were calculated for 300 keV electrons at an collection of 10 mrad.

excess of oxygen. The oxygen in the grain interior is barely detectable, while strong oxygen peaks were observed at the boundaries. The concentration ratio of oxygen to boron N^O/N^B at the two boundaries were determined to be 0.451 and 0.702, more than one order of magnitude higher than at the GIs. The high concentration of oxygen may be associated with an oxide wetting-phase lying between poorly sintered MgB_2 grains. It may be formed by oxidation of Mg vapor at high temperatures during sintering.

The fine structure of the boron K pre-edge was also studied using high-resolution EELS for large-angle structurally intact grain boundaries. Fig. 12 is an example revealing the difference between the fine structure at the GB and at the GI. The sharp boron peak at 202 eV is accompanied by a broad peak centered at 223.5 eV. The spectra were acquired from relatively thick areas, $1.8\lambda_m$ and $1.6\lambda_m$, respectively, in order to maximize the interfacial volume with respect to the volume of the amorphous layers formed during ion milling at the top and bottom surfaces of the sample.

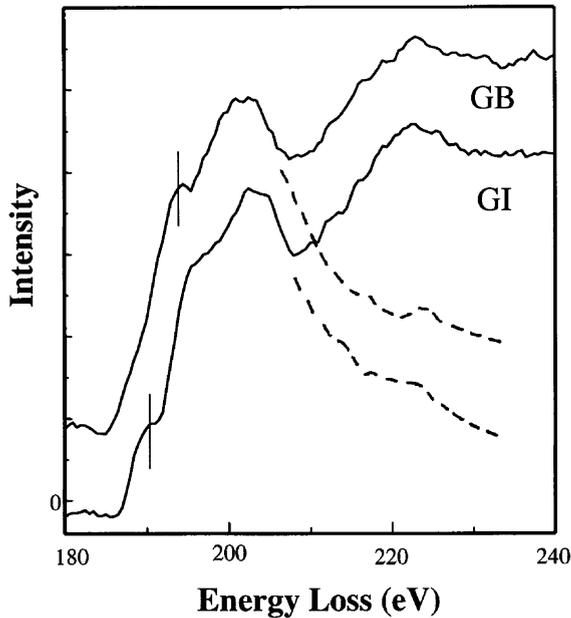


Fig. 12. Nano-probe EELS showing the fine structure of the boron K-edge acquired from a GB and GI (GI, 50 nm away from the GB). Note the change of the core-loss intensity of the pre-peak marked by the vertical thin lines in the spectra. The dashed lines represent the spectra after plural scattering removal.

Fortunately, plural scattering from a thick region has little effect on the pre-edge fine structure of an elemental edge. On the other hand, it can significantly modify the core-loss intensities above 210 eV, since the first plasmon peak of MgB_2 is at 20 eV. The dashed lines in the spectra represent the core-loss intensity of the post-edge after the removal of the plural scattering, based on the Fourier-ratio deconvolution method, i.e., the spectrum Fourier transform is divided by the low-loss Fourier transform, followed by an inverse Fourier transform. It is interesting to note that there are two weak peaks in the boron pre-edge spectra at about 190.5 and 194.5 eV, respectively. The former is seen only in the spectrum acquired from the GI, while the latter is more clearly visible from the grain boundary. The change in the boron pre-peak intensity may be related to a change of hole concentration in the area. Like $\text{YBa}_2\text{Cu}_3\text{O}_7$, MgB_2 is considered to be a hole-doped superconductor, based on Hall effect measurements [13]. In

$\text{YBa}_2\text{Cu}_3\text{O}_7$, the change in pre-peak intensity of the oxygen K-edge at 528 and at 530 eV was related to the boundary superconductivity and weak-link behavior [19,20]. The former corresponds to the hole density ($1s \rightarrow 2p$ transition) and attains a maximum for optimum superconductivity, while the later is associated with a hybridized d state ($1s \rightarrow 3d$ transition), and has a maximum intensity in the insulating non-superconducting regime. Recently, An and Pickett [10] calculated the effects of various phonon modes of the electronic structure of MgB_2 . They concluded that superconductivity results almost exclusively from in-plane boron bands that contribute strongly to the Fermi-level density of states because of the two-dimensional nature of the material. They found that there are non-bonding π band (p_z) and bonding σ band (sp_xp_y) associated with boron atoms, and that the σ to π charge-transfer results in hole doping. In their calculations the σ band extends to about 1 eV above the Fermi level. We believe this is the feature we observe at 190.5 eV (we assume the B K-edge onset at 188 eV), which is then associated with variation in the hole concentration. The lack of the pre-peak intensity at the boundary resembles the situation in the $\text{YBa}_2\text{Cu}_3\text{O}_7$ where the disappearance of the pre-edge at the oxygen K-edge is the signature of a GB with degraded superconducting properties. A systematic study in MgB_2 , ideally using bicrystals, of electronic structure and superconductivity of GBs, has not yet been conducted. If the boundaries are strongly coupled, as reported in Refs. [2,3], it suggests that the width of the interfacial hole-depletion region may be smaller than the coherence length of MgB_2 , which was estimated to be 5 nm [2,21]. Optimistically, the hole deficiency might enhance flux pinning at the boundaries. At any rate, it is likely that such hole-density variations will have a profound effect on superconducting transport properties across the boundaries in this binary intermetallic compound.

4. Conclusions

The structural defects in sintered MgB_2 have been analyzed. The major second phase was found

to be MgO particles with a wide size distribution, ranging from 10 to 500 nm in diameter. Depending on their crystallographic orientation relative to the MgB₂ matrix, these MgO particles can generate dislocations. Most dislocations observed were perfect dislocations with a Burger vector $\mathbf{b} = [100]$ or $[010]$, lying in the basal plane. Stacking faults bounded with a pair of partial dislocations were also observed. Although both second-phase particles and dislocations can act as strong pinning centers, the pinning strength from dislocations and stacking faults are likely to be confined within the a - b planes, i.e., being weak for flux lying in the a - b plane, but strong along the c -axis. GBs in MgB₂ often have this basal plane as their boundary plane, consistent with the weak bond between boron and magnesium atoms. An excess of Mg was observed even in structurally intact GBs. High-resolution EELS revealed that there is a change at the onset of the boron K-edge at the grain boundaries compared with that from the GIs, suggesting a change of the electronic structure that was modified by the Mg–B bonding at the interfaces. Since the correct density of states near the Fermi level is required to achieve superconductivity, a reduction in states may significantly alter the transport properties across the boundaries. This phenomenon may be similar to the change of the intensity of pre-peaks at the oxygen K-edge across the GBs in YBa₂Cu₃O₇.

Acknowledgements

This work is supported by US Department of Energy, Division of Materials, Office of Basic

Energy Science, under contract no. DE-AC02-98CH10886.

References

- [1] J. Nagamasu et al., Nature (London) 410 (2001) 63.
- [2] P.C. Canfield, D.K. Finnemore et al., Phys. Rev. Lett. (2001) cond-mat/0102289.
- [3] D.C. Larbalestier, M.O. Rikel et al., Nature, in press.
- [4] M. Kambara, et al., Supercond. Sci. Tech. 14 (2001) L5.
- [5] C.B. Eom et al., Nature, in press.
- [6] S. Pataik, et al., Supercond. Sci. Tech. 14 (2001) 315.
- [7] J.S. Slusky, et al., Nature 410 (2001) 343.
- [8] S. Jin, H. Marvori, R.B. van Dover, cond-mat/0104236.
- [9] J.D. Jorgensen, D.G. Hinks, S. Short, cond-mat/0103069.
- [10] J.M. An, W.E. Pickett, Phys. Rev. Lett. 86 (2001) 4366.
- [11] J.Q. Li, L. Li, Y.Q. Zhou, Z.A. Ren, G.C. Che, Z.X. Zhao, cond-mat/0104350.
- [12] T. Vogt et al., Phys. Rev. Lett., cond mat/0102480, in press.
- [13] W.N. Kang, C.U. Jung, K.H.P. Kim, M. Park, S.Y. Lee, H. Kim, E. Choi, K.H. Kim, M. Kim, S. Lee, cond-mat/0102313.
- [14] K.E. Spear, J. Less-Comm. Metals 47 (1976) 195.
- [15] P.B. Hirsch, A. Howie, R.B. Nigholson, D.W. Pashley, Electron Microscopy of Thin Crystals, Butterworths, London, 1965.
- [16] R.F. Egerton, Electron Energy-Loss Spectroscopy in the Electron Microscope, Plenum Press, New York, 1996.
- [17] M. Suenaga, W. Jansen, Appl. Phys. Lett. 43 (1983) 791.
- [18] D.O. Welch, IEEE Trans. Magn. 21 (1985) 827.
- [19] A.R. Moodenbaugh, D.A. Fischer, Physica C 230 (1994) 177.
- [20] Y. Zhu, J.M. Zuo, A.R. Moodenbaugh, M. Suenaga, Philo. Magn. A 70 (1994) 969.
- [21] D.K. Finnemore, J.E. Ostenson, S.L. Bud'ko, G. Lapertot, P.C. Canfield, con-mat/0102114.